Supporting Information

High-Valent Iron Single-Atom Catalysts for Improved Overall Water Splitting via Reducing Energy Barrier and Stabilization of Active Center

Ayyavu Shankar,[§] Sundaramoorthy Marimuthu,[§] and Govindhan Maduraiveeran*

Materials Electrochemistry Laboratory, Department of Chemistry, College of Engineering and Technology, SRM Institute of Science and Technology, Kattankulathur- 603 203, Chengalpattu, Tamil Nadu, India

[§]Equal Contribution

*Correspondence E-mail: maduraig@srmist.edu.in

Experimental Procedures

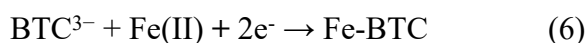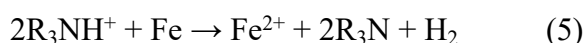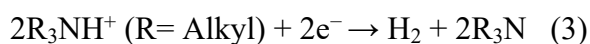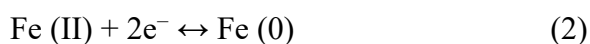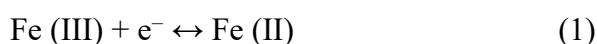**Materials.** Anhydrous Iron Chloride ($FeCl_3$) was purchased from Sigma-Aldrich. 1,3,4-Benzenetricarboxylic Acid (1,3,4-H_3BTC), Nafion solution (1 wt%), and KOH (99%, AR grade) were purchased from Sigma-Aldrich. Triethylamine Hydrochloric Acid (TEA) and N, N-dimethylformamide (DMF) were purchased from Alfa Aesar. All chemicals were used directly without further purification. Milli-Q water with 18.2 MΩ cm was collected from a NANO pure Diamond UV ultrapure water purification system, which was employed to prepare all the experimental solutions involved in this study.

Fabrication of the Fe-SACs electrodes

Electrochemical deposition method was employed to prepare a series of nanostructured Fe-SACs catalyst on carbon modified nickel nanosheets (C-Ni NS). A section of ~0.05 cm diameter, and ~0.2 cm length x ~0.2 cm breath of nickel foam (NF) with a geometric surface area of ~0.12 cm^2 area was exposed to the electrolyte solution. Ahead of the electrochemical deposition, the NF was cleaned via sonication for 15 min sequentially in hydrochloric acid, water and acetone. Typically, cyclic voltammograms (CVs) were performed for the bare NF in a precursor mixture of different Fe concentrations (0:25(**1**), 0.50(**2**), 1.0(**3**), 1.25(**4**), 1.50(**5**)) mM in N, N-dimethylformamide (DMF) for five incessant cycles with low scan rate (5.0 mVs^{-1}) in the range of ~-0.16 to ~1.63 V against RHE (Scheme S1). The as-developed Fe-SACs|C-Ni electrodes were represented as Fe-SACs|C-Ni @**1**, Fe-SACs|C-Ni@**2,** Fe-SACs|C-Ni@**3**, Fe-SACs|C-Ni@**4** and Fe-SACs|C-Ni@**5**, respectively. For the comparison purpose, other single-metal atom catalysts, such as Co-SACs|C-Ni, Ni-SACs|C-Ni, and Cu-SACs|C-Ni were developed by varying the metal precursors under similar experimental conditions.

The precursor solution stability can be attributed to strong contacts between DMF molecules and Fe^{3+} ions, as well as the development of hydrogen-bonded DMF and H_3BTC

structures. A pair of redox waves were seen when Et_3NHCl was used as a probase. Et_3NH^+ can be reduced to Et_3N and H_2 (Equation (3)),[1] as previously described. The reduction of Et_3NHCl increases the local pH near the cathode surface, which results in faster in situ deprotonation of ligands and end-up much better and more rapid formation of MOF films on the electrode. The CV of adding H_3BTC to Et_3NHCl/DMF solution was studied, where the response for H^+ reduction at 0.9 V increased but the peak potential did not shift, indicating that H_3BTC and Et_3NHCl deprotonation in DMF solution transpired at around 0.9 V, as given as follows:

$$Fe\ (III) + e^- \leftrightarrow Fe\ (II) \qquad\qquad (1)$$

$$Fe\ (II) + 2e^- \leftrightarrow Fe\ (0) \qquad\qquad (2)$$

$$2R_3NH^+\ (R= Alkyl) + 2e^- \rightarrow H_2 + 2R_3N \quad (3)$$

$$H_3BTC + 3R_3N \rightarrow BTC^{3-} + 3R_3NH^+ \qquad (4)$$

$$2R_3NH^+ + Fe \rightarrow Fe^{2+} + 2R_3N + H_2 \qquad (5)$$

$$BTC^{3-} + Fe(II) + 2e^- \rightarrow Fe\text{-}BTC \qquad (6)$$

The state-of-the-art RuO_2 catalyst ink was created by dispersing ~5.0 mg of the catalyst in 0.5 mL DI water with ~1.0% Nafion. The catalyst ink was thoroughly distributed by employing an ultrasonication for about three minutes. The catalyst ink (about ~10 µL) was drop casted onto a nickel foam surface, and allowed to air dry.

Materials Characterisation

The surface morphology and elemental composition were investigated energy dispersive X-ray (EDX) methods using high-resolution scanning electron microscopy (HR-SEM, FEI QUANTA 200). Transmission electron microscopic (TEM) measurements were carried out using of a JEOL 2010F TEM. In order to study the X-ray diffraction (XRD) patterns, a PANanalyticalXpert Pro diffractometer with a monochromatic Cu Kr (1.5406, 2.2 KW Max) filter was used. Chemical compositions of metal ions were determined by PERKIN ELMER

OPTIMA 5300 DV inductively coupled plasma optically emission spectrometer (ICP-OES). X-ray photoelectron spectroscopy (XPS-PHI Versa probe III) was used to investigate chemical state and chemical composition analysis. LABRAM HR Evolution (HORIBA France) with a wavelength of 532 nm and a power of 3 mW is used to acquire the Raman spectra. A Fourier Transform Infrared Tracer-100AH FT-IR spectrometer was used to perform Fourier Transform Infrared Spectroscopy (FT-IR). The Raman spectra are obtained using LABRAM HR Evolution (HORIBA France) with the wave-length 532 nm and power of 3 mW. UV-vis absorption spectral studies were conducted at room temperature by an UV-vis-NIR Cary 5000 spectrophotometer.

Electrochemical Measurements

The electrocatalytic characteristics of the samples were assessed using a Biologic electrochemical workstation (VSP-300). The electrocatalytic tests were carried out at room temperature in a conventional three-electrode configuration. The nickel foam (NF) was employed as the working electrode (geometric area: ~0.12 cm^2). The counter electrode was a platinum wire. The reference electrode was an Ag/AgCl electrode. All potentials described in this paper were calculated using the formula E (V vs. RHE) = E (V vs. Ag/AgCl) + 0.197 V + 0.0591pH. Using a linear sweep voltammetry technique, the OER polarisation curves were measured in 1.0 M KOH. Prior to the assessment of electrochemical performance, several CV scanning cycles were performed to stabilize the catalysts.

Calculation Method

Turn over frequency (TOF) value was calculated based on the equation of "jS/4Fm"[2,3] for each active site, where "S" represents the electrode's geometric surface area, "F" means the Faraday constant, and "m" is the number of moles of metals on the electrode. In the equation,

"*j*" is the current density at a specific overpotential. Tafel slope (b) was calculated by fitting polarisation curve data to the Tafel equation of a + b log |j|,[4] where *j* is the current density at the specified overpotential and "a" and "b" are Tafel constants. "η" represents the overpotential for OER/HER. Electrochemical impedance spectroscopy (EIS) measurements were held within the frequency scan between 50 mHz to 100 kHz. The mass loading of Fe-SACs|C-Ni@**1**, Fe-SACs|C-Ni@**2**, Fe-SACs|C-Ni@**3**, Fe-SACs|C-Ni@**4**, and Fe-SACs|C-Ni@**5** electrodes were estimated to be 16.6, 19.1, 20.8, 27.5 and 41.6 mg cm^{-2}.

Double-layer capacitance (C_{DL}) was determined from the slope of charging currents (i_c) as a function of scan rate (v), as shown in Eqn. (7). This was done to determine the average absolute value of the cathodic and anodic slopes of the linear fitting of the plot.[5]

$$i_c = vC_{DL} \tag{7}$$

The electrochemical double-layer capacitance for the Fe-SACs|C-Ni@**3** catalyst obtained from the scan-rate investigation was C_{DL}=11.74 mF cm^2. Using eqn. (8), the electrochemically active surface area (ECSA) of Fe-SACs|C-Ni@**3** was calculated from the catalytic surface's electrochemical double-layer capacitance.[6]

$$ECSA = C_{DL}/C_s \text{ x A} \tag{8}$$

The electrochemically active surface area of Fe-SACs|C-Ni@**3** was calculated using the double layer capacitance (C_{dl}), A is the electrode area (1 cm^2 for our working electrodes) and specific capacitance C_s value of 1.0 M KOH. The specific capacitance of the sample or the capacitance of a planar surface per unit area under the same electrolyte conditions was reported to be 0.040 mF. Additionally, using Eqn. (9), the roughness factor (RF) of the Fe-SACs|C-Ni@**3** electrode can be calculated.[7]

$$RF = ECSA/GSA \tag{9}$$

where GSA stands for geometric surface area, the catalytic material used in this study had a geometric surface area of 0.12 cm². Then, the working electrode Fe-SACs|C-Ni@**3** roughness factor (RF) was measured.

The number of active sites were calculated following the method described by[2]. In detail, CVs were recorded in a 1.0 M alkaline KOH in a potential window of -0.3 to 0.6 V vs. Ag/AgCl at a scan rate of 20 mV s⁻¹. Integrating the area under the voltage vs. current density gives the voltammetric charge, which was used to determine the number of active sites in eqn. (10).

$$n = Q/4F \qquad (10)$$

Where

"n" is the number of active sites (moles)

"Q" is voltammetric charge

"F" is the Faraday constant (96,480 C/mol)

"4" is the number of electrons transferred during OER.

To access the intrinsic activity of the as-obtained samples, both mass activities and TOFs were computed by eqns. (11) and (12):[6]

$$\text{Mass activity} = (j \times A)/ m \qquad (11)$$

$$TOF = \frac{JS}{4F_n} \qquad (12)$$

Where j was the current density, A was the geometric surface area of the electrode, F was the faraday constant (96,485 C mol⁻¹) and S is the area of the electrode, j is the current density at obtained overpotential for both OER and HER in A cm², F is the Faraday constant of 96485 C mol⁻¹, and n is the quantity of moles of the active materials placed onto the NF.

Table S1. List of the weight percentage of Fe in Fe-SACs|C-Ni@**1**, Fe-SACs|C-Ni@**2**, Fe-SACs|C-Ni@**3,** Fe-SACs|C-Ni@**4** and Fe-SACs|C-Ni@**5** materials from ICP-OES measurements.

Materials	ICP-OES (Wt. %) µg/mL
	Iron
Fe-SACs|C-Ni@**1**	2.5
Fe-SACs|C-Ni@**2**	3.8
Fe-SACs|C-Ni@**3**	6.7
Fe-SACs|C-Ni@**4**	3.7
Fe-SACs|C-Ni@**5**	5.5

Table S2. Elemental values of the Fe-SACs|C-Ni@**1** (a), Fe-SACs|C-Ni@**2** (b), Fe-SACs|C-Ni@**3** (c), Fe-SACs|C-Ni@**4** (d) and Fe-SACs|C-Ni@**5** (e) electrodes, which were derived from **Figs. 3c and S17**.

Electrodes	E_{app}(V) vs. *RHE*	R_s [Ω]	R_p [Ω]	*CPE* Q_1 [F/s]	*CPE* Q_2 [F/s]
Fe-SACs|C-Ni@**1**		3.75	84.18	9.51×10^{-6}	4.737×10^{-3}
Fe-SACs|C-Ni@**2**		3.77	63.37	8.95×10^{-6}	5.356×10^{-3}
Fe-SACs|C-Ni@**3**	1.50	3.47	9.82	1.75×10^{-3}	0.026
Fe-SACs|C-Ni@**4**		5.40	26.34	1.11×10^{-3}	9.97×10^{-3}
Fe-SACs|C-Ni@**5**		5.03	21.41	42.07×10^{-6}	0.016

Table S3. Comparative electrocatalytic performance of Fe-SACs|C-Ni@**3** to recently reported electrocatalysts for HER, OER and overall water splitting electrocatalysts.

S. No	Electrocatalyst	η_{HER} (mV)	η_{OER} (mV)	Cell Voltage (U_{cell})	Ref.
1	NiFe@NC/NGC	190	287	1.63	8
2	*a*-CoSe/Ti	121	292	1.65	9
3	NiFe-NCs	197	271	1.67	10
4	CoSx	102	284	1.64	11
5	Co-Co$_2$C/CC	096	261	1.63	12
6	VOOH	164	270	1.62	13
7	NC@CuCo$_2$N*x*/CF	105	230	1.62	14
8	Co$_9$S$_8$	217	299	1.66	15
9	CoS/MoS$_2$	180	281	1.61	16
10	NiCoP NWAs/NF	197	370	1.64	17
11	cobalt iron phosphate	55	251	1.75	18
12	**Fe-SACs|C-Ni@3**	164	246	1.60	**This Work**
NGC: Nitrogen-Doped Graphitized carbon; NCs: Nano Cubes; CC: Carbon Cloth; CF: Carbon Fibre; NWAs: Nano Wire Arrays; NF: Nickel Foam					
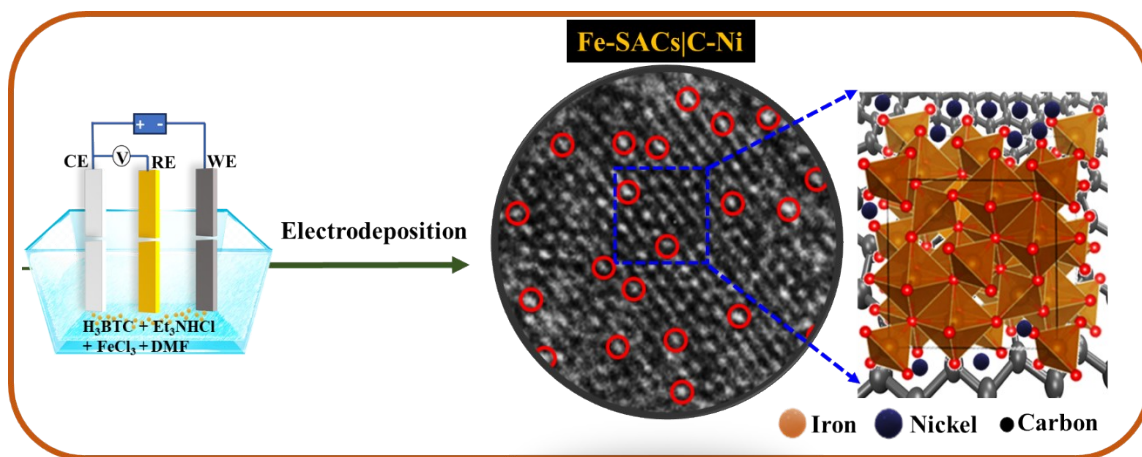
Scheme S1. Pictorial illustration for fabricating Fe-SACs|C-Ni electrode materials.

OER Reaction Pathway

HER Reaction Pathway
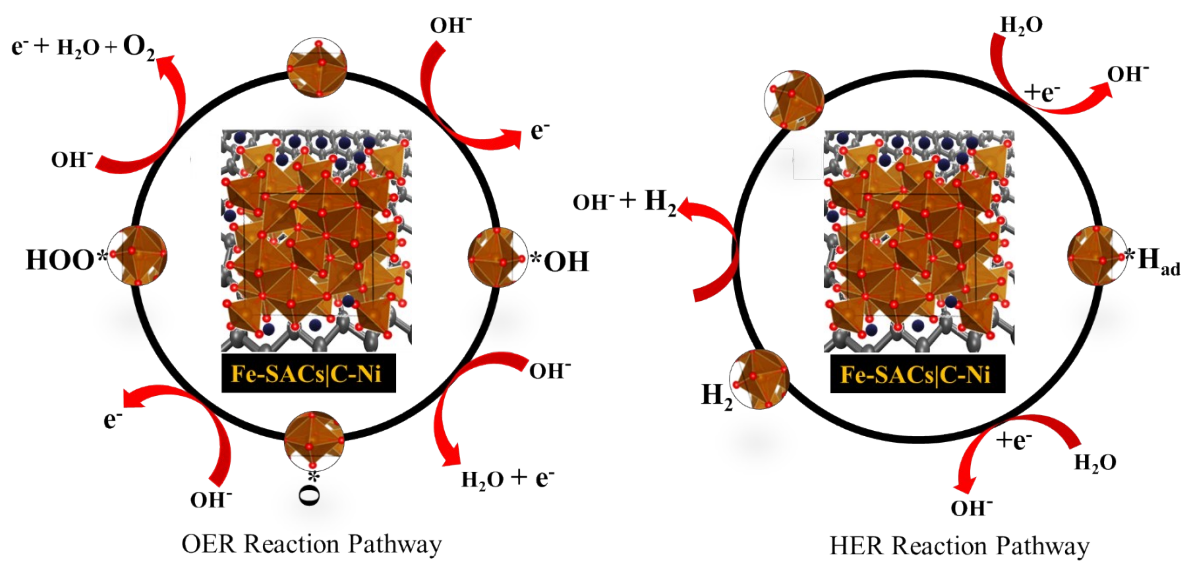
Scheme S2. OER and HER reaction pathways at Fe-SACs|C-Ni electrode materials.
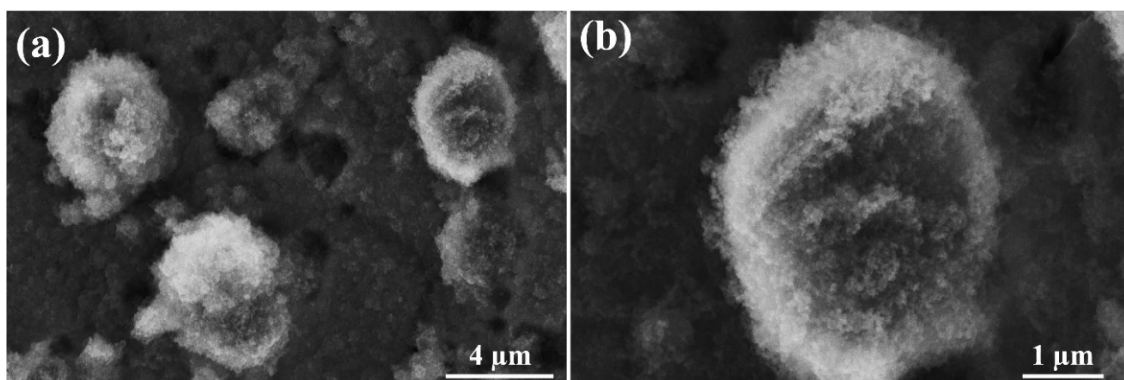
Fig. S1. SEM images of the Fe-SACs|C-Ni@**3** electrode with different magnifications.
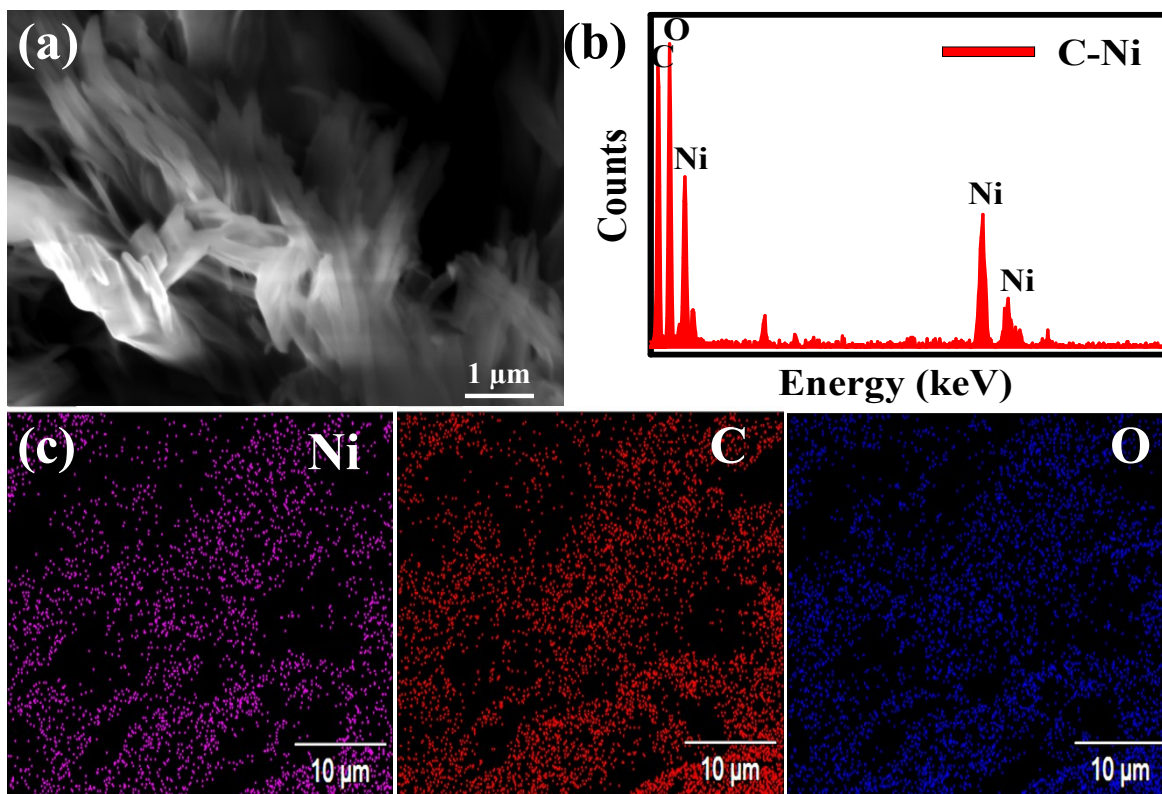
Fig. S2. SEM image (a), SEM-EDX spectrum (b), and elemental mapping (c) of the carbon-nickel (C-Ni) nanosheets.
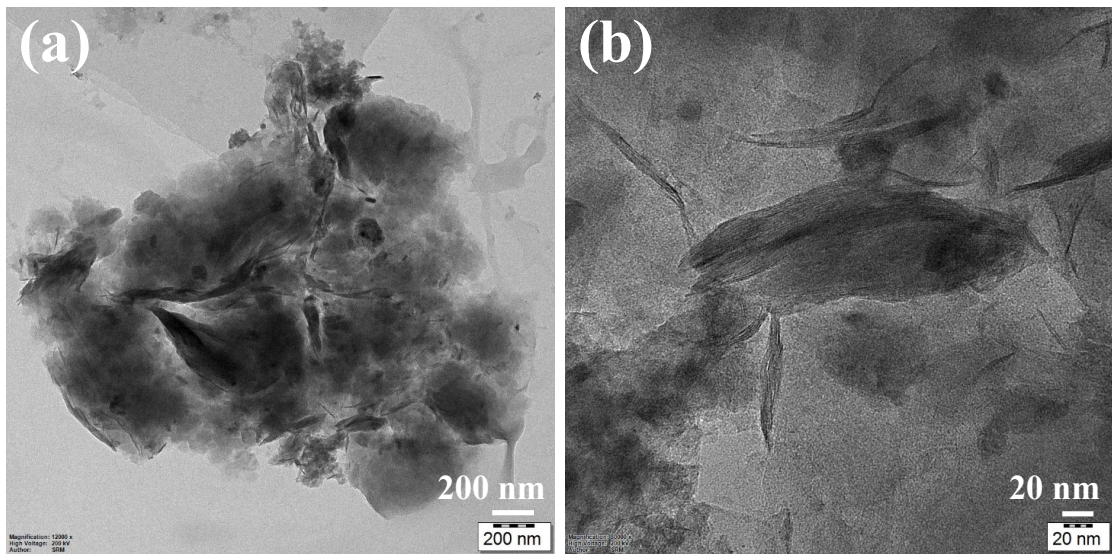
Fig. S3. TEM images of the carbon-nickel (C-Ni) nanosheets electrode.
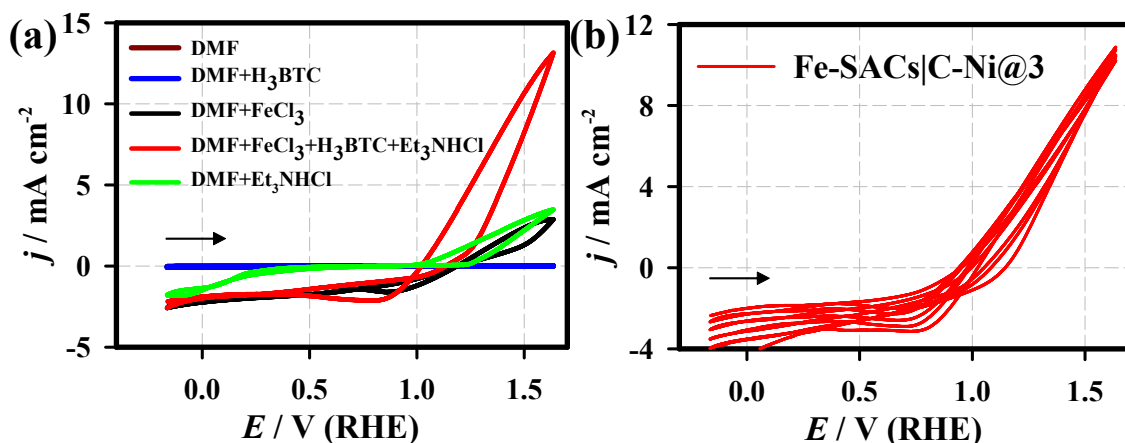
Fig. S4. CV curves of the nickel foam electrode recorded in DMF background solution (brown) and those containing H_3BTC (1 mM, blue), $FeCl_3$ (1 mM, black), Et_3NHCl (1 mM, green) and a mixture of H_3BTC (1 mM), Et_3NHCl (1 mM) and $FeCl_3$ (1 mM) (red), respectively, measured at 30°C with Et_3NHCl (1 mM), as the supporting electrolyte and scan rate of 5 mV s^{-1} (a); CV curves of DMF background solution (brown) and a mixture of H_3BTC (1 mM), and $FeCl_3$ (1 mM), respectively, measured at 30°C with Et_3NHCl (1 mM), as the supporting electrolyte and scan rate of 5 mV s^{-1} (b).
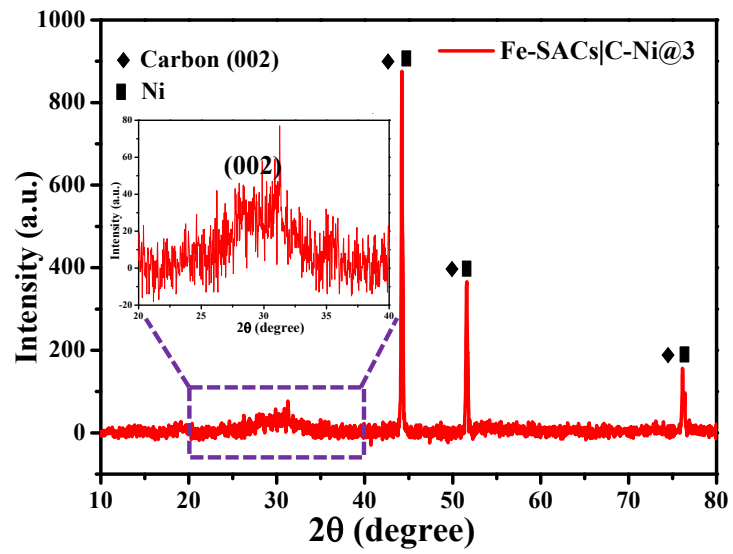
Fig. S5. XRD pattern of Fe-SACs|C-Ni@**3** electrodes. Rectangle symbol denotes as substrate Ni peaks.
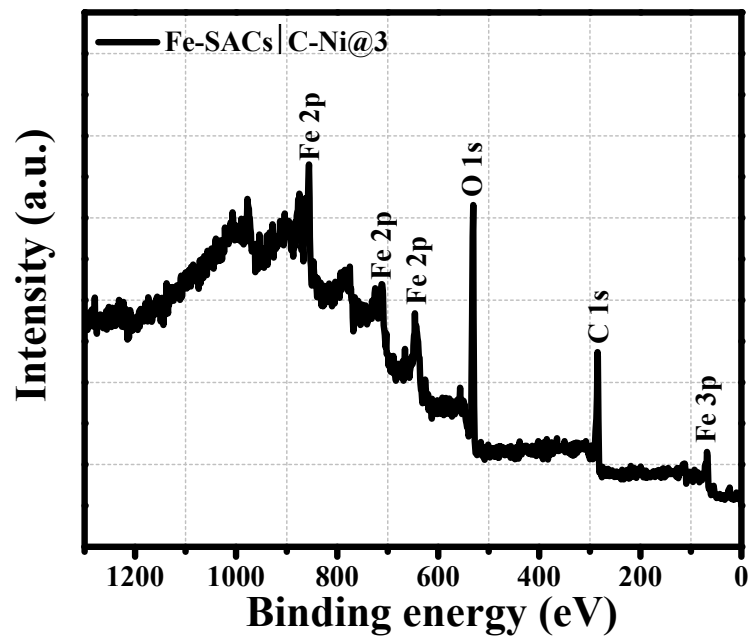
Fig. S6. XPS survey spectrum of Fe-SACs|C-Ni@**3** electrode.
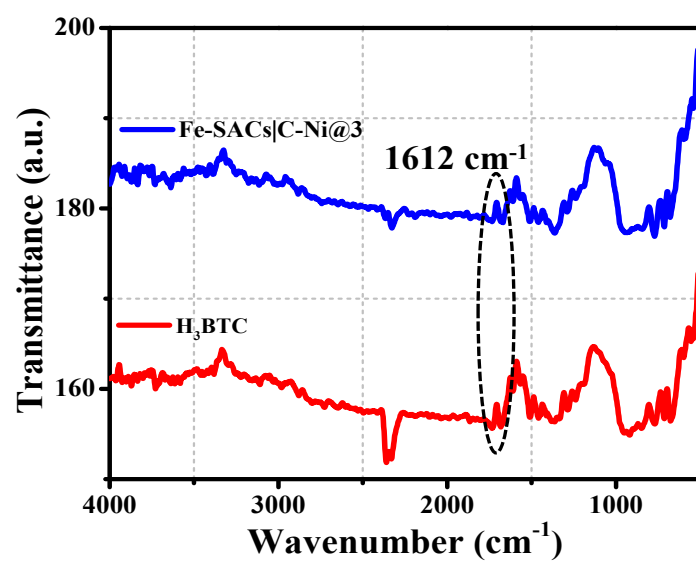
Fig. S7. FT-IR spectra of Fe-SACs|C-Ni@**3** and H$_3$BTC materials.
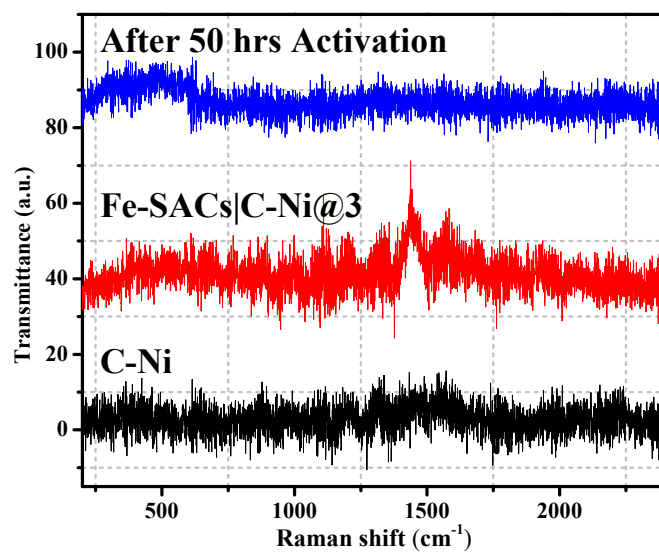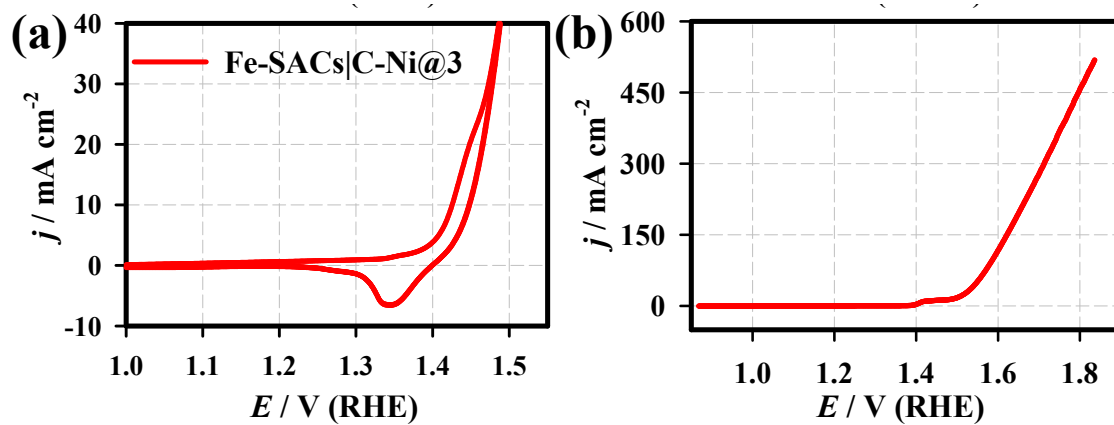
**Fig. S8.** Raman spectra of Fe-SACs|C-Ni@**3** and H$_3$BTC electrodes.
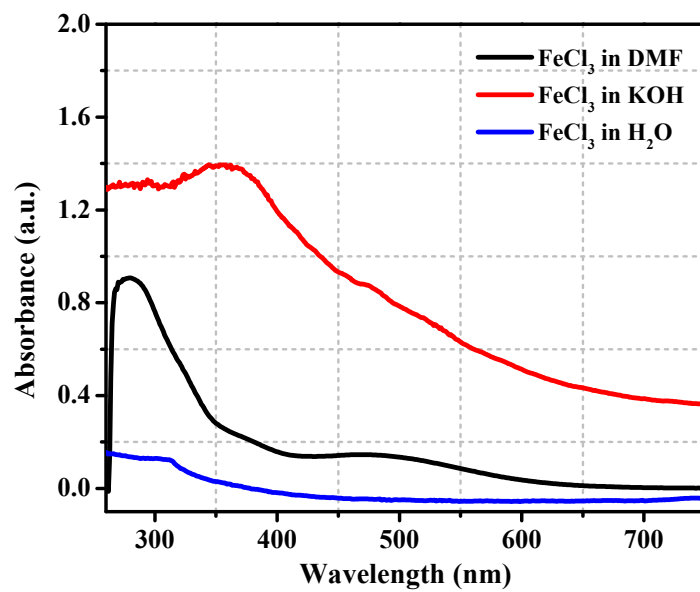
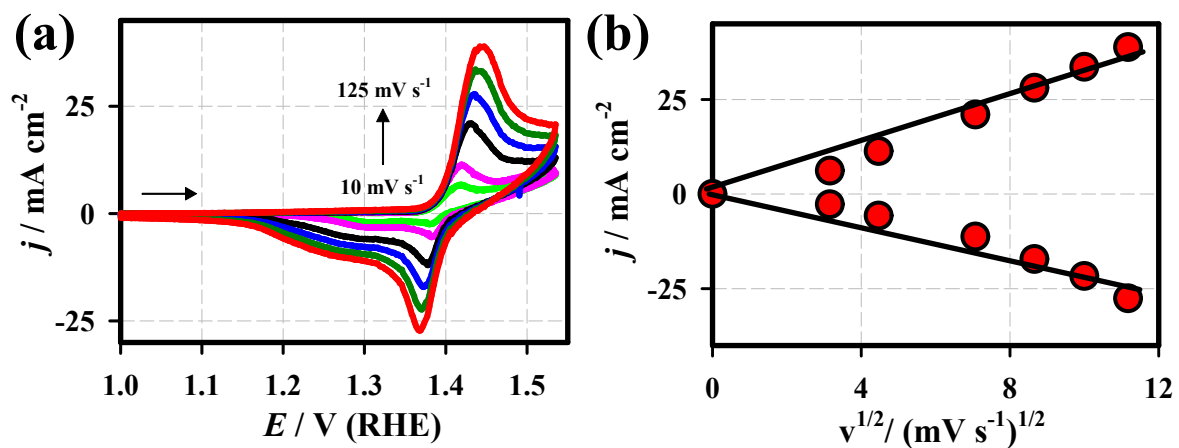**Fig. S9.** UV-vis spectra of aqueous solution containing 1.0 mM FeCl$_3$.
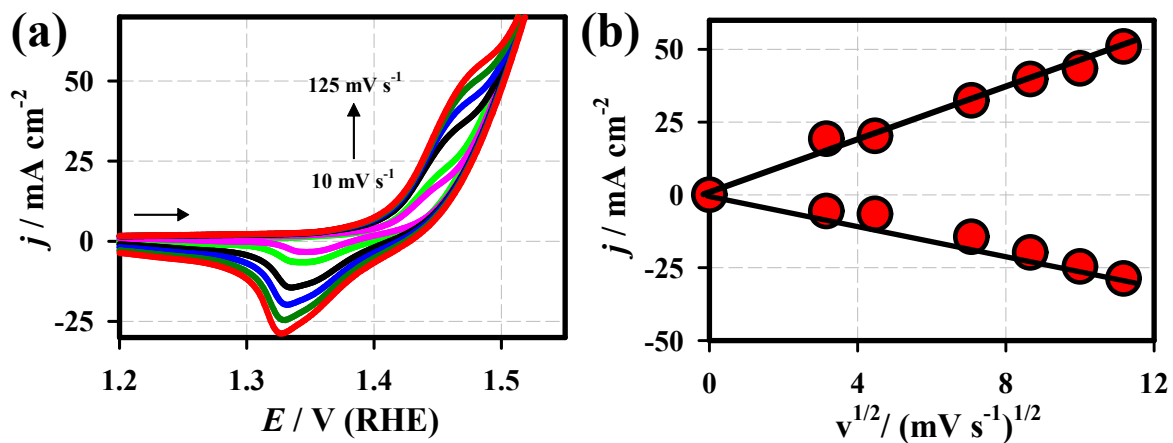
Fig. S10. CV curves of the Fe-SACs|C-Ni@**3** electrode recorded in 1.0 M KOH at different scan rates from 10 to 125 mV s^{-1} (a). The plot of capacitance current against the square root of the scan rates (b).

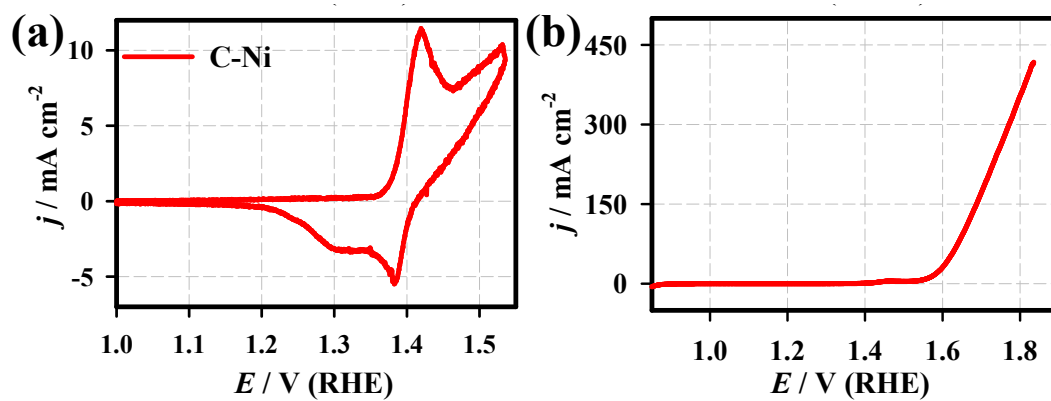**Fig. S11.** CV (a) and LSV (b) curves of the Fe-SACs|C-Ni@**3** electrode recorded in 1.0 M KOH at the scan rate of 10 mV s^{-1}.
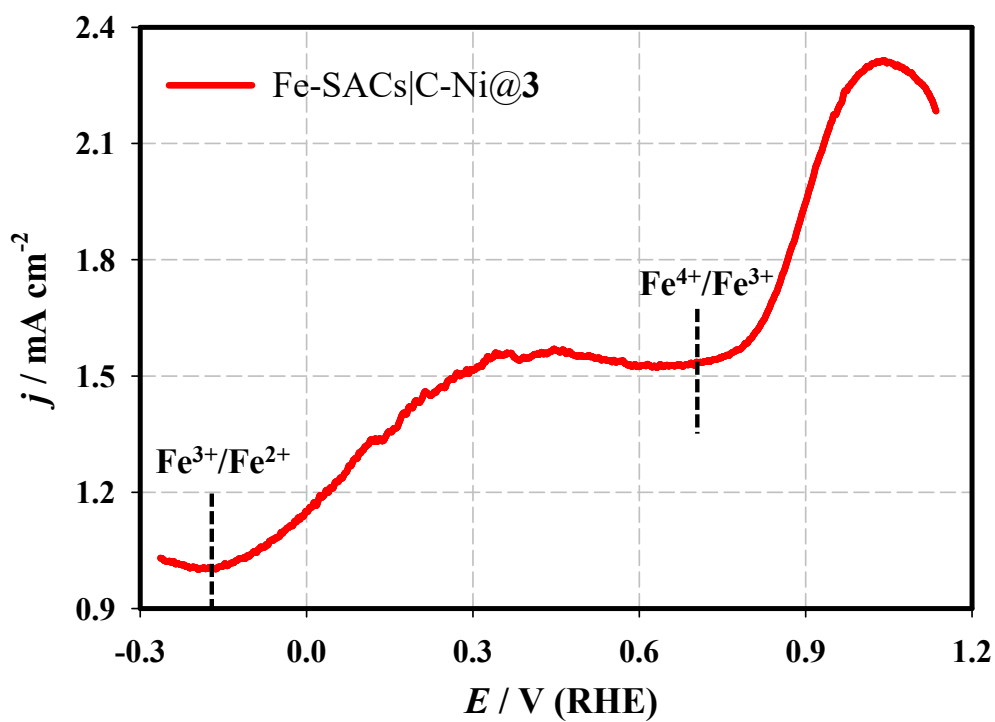
**Fig. S12.** Differential pulse voltammogram (DPV) of Fe-SACs|C-Ni@**3** in DMF at the scan rate of 5.0 mV s^{-1}.

Fig. S13. CV curves of the carbon-nickel (C-Ni) nanosheets electrode recorded in 1.0 M KOH at different scan rates from 10 to 125 mV s^{-1} (a); The plot of anodic, and cathodic current densities against the square root of the scan rates (b).

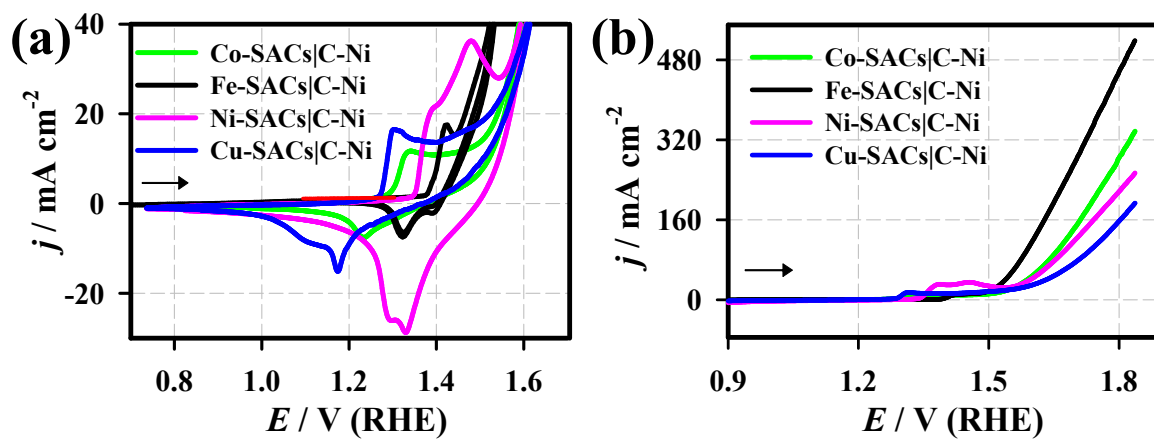**Fig. S14.** CV (a) and LSV (b) curves of the carbon-nickel (C-Ni) nanosheets electrode recorded in 1.0 M KOH at the scan rate of 10 mV s^{-1}.
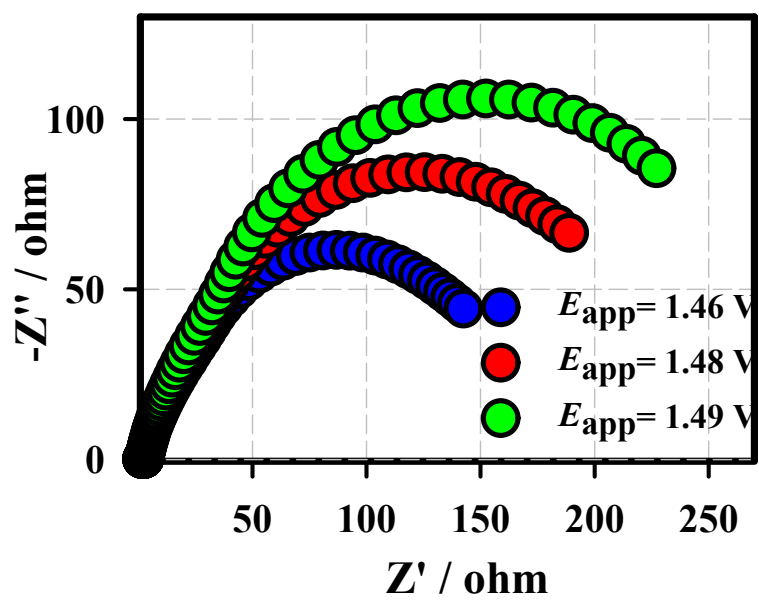
Fig. S15. Nyquist plots of the carbon-nickel (C-Ni) nanosheets electrode under the various E_{app}.

Fig. S16. CV (a) and LSV (b) curves of the Fe-SACs|C-Ni (black), Co-SACs|C-Ni (green), Ni-SACs|C-Ni (pink), and Cu-SACs|C-Ni (blue) electrodes recorded in 1.0 M KOH at the scan rate of 20.0 mV s^{-1}.
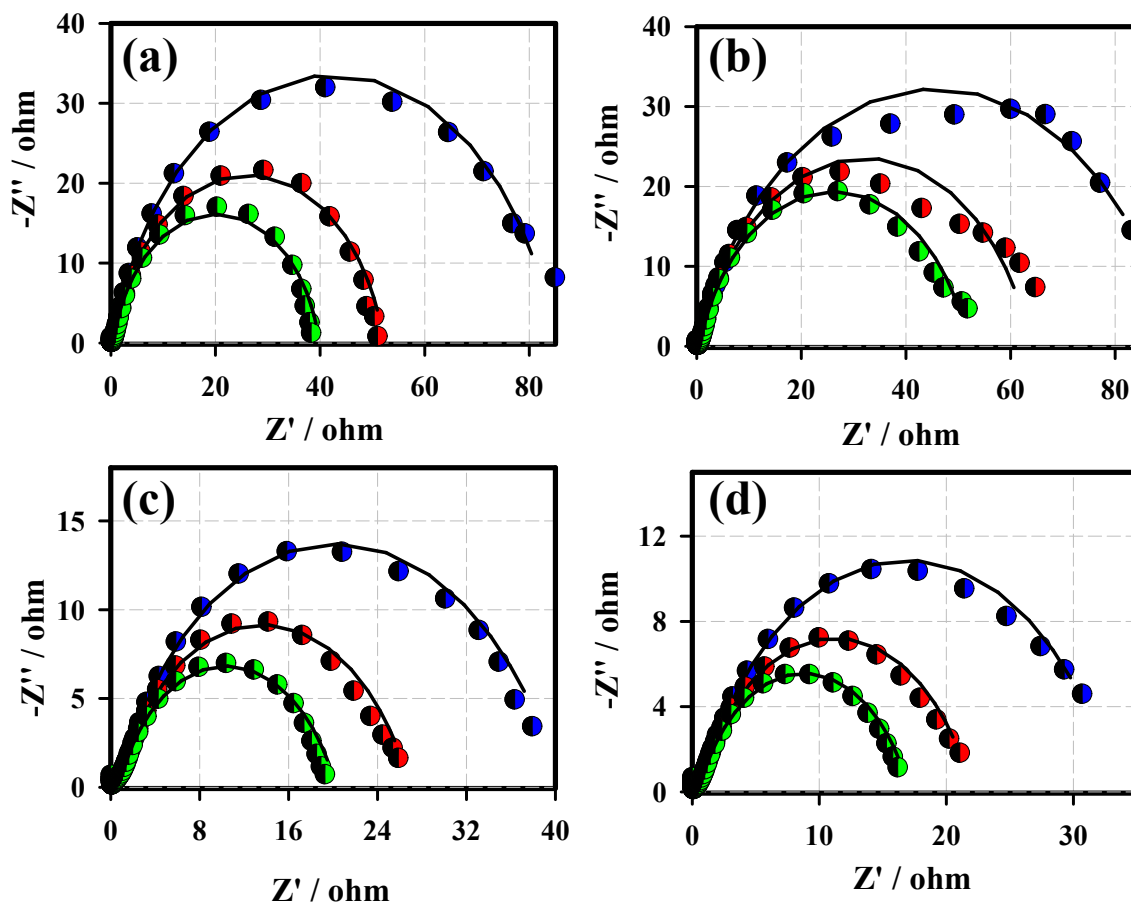
Fig. S17. Nyquist plots of the nanostructured Fe-SACs|C-Ni@**1** (a), Fe-SACs|C-Ni@**2** (b), Fe-SACs|C-Ni@**4** (c) and Fe-SACs|C-Ni@**5** (d) electrodes recorded at the AC amplitude of 1.48 V (blue curve), 1.49 V (red curve) and 1.51 V (green curve) in 1.0 M KOH. The solution resistance (R_s) was obtained from the semicircle intersection at the real high-frequency axis, and the polarization resistance (R_p) at the low frequency near the electrode-electrolyte interface. The charge transfer resistance (R_{ct}) was calculated from the difference in R_p and R_s.
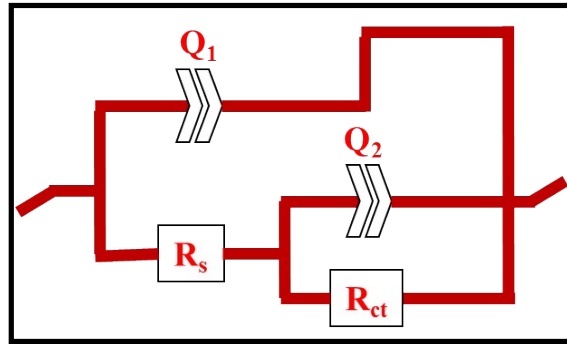
Fig. S18. EIS Nyquist plots of the fitted equivalent circuit for **Figs. 2(c), 3(c), S15,** and **S17.**
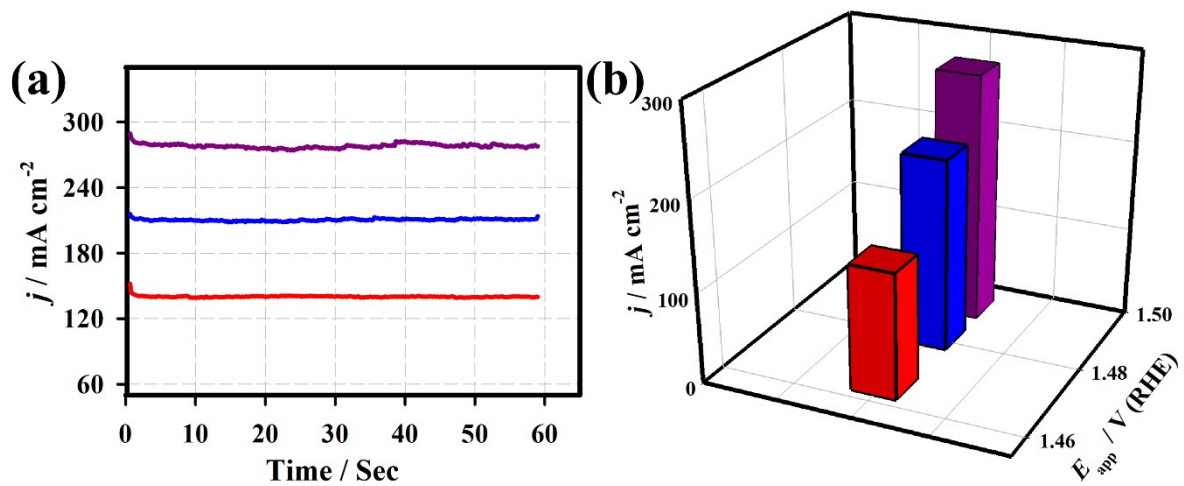
Fig. S19. Chronoamperometric response of the Fe-SACs|C-Ni@**3** electrode under the applied electrode potentials of 1.48 V, 1.49 V, and 1.50 V (a); Corresponding bar diagram (b).
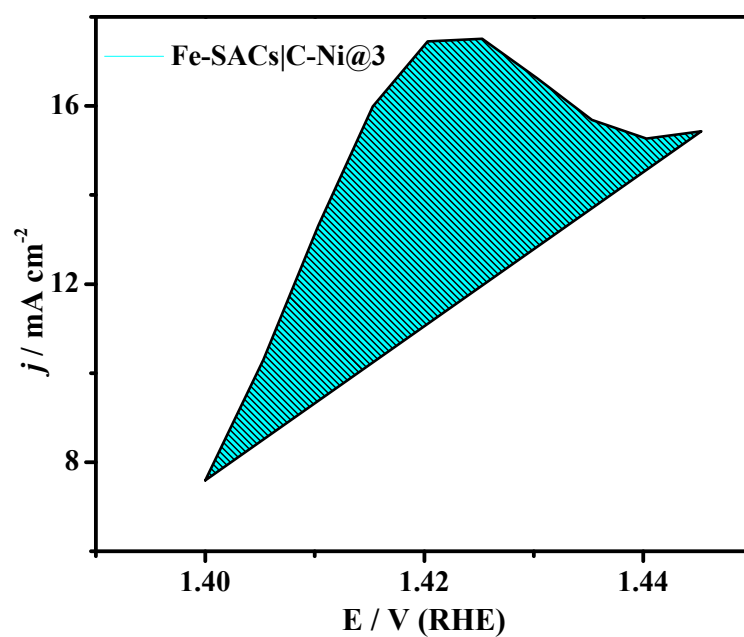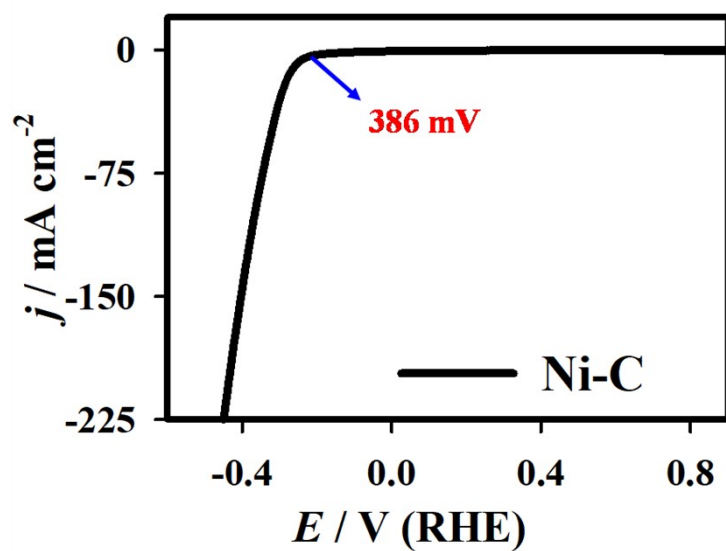
Fig. S20. The isolated oxidation peaks of the same CV used for charge integration and the calculation of the number of active sites at the Fe-SACs|C-Ni@**3** electrode.
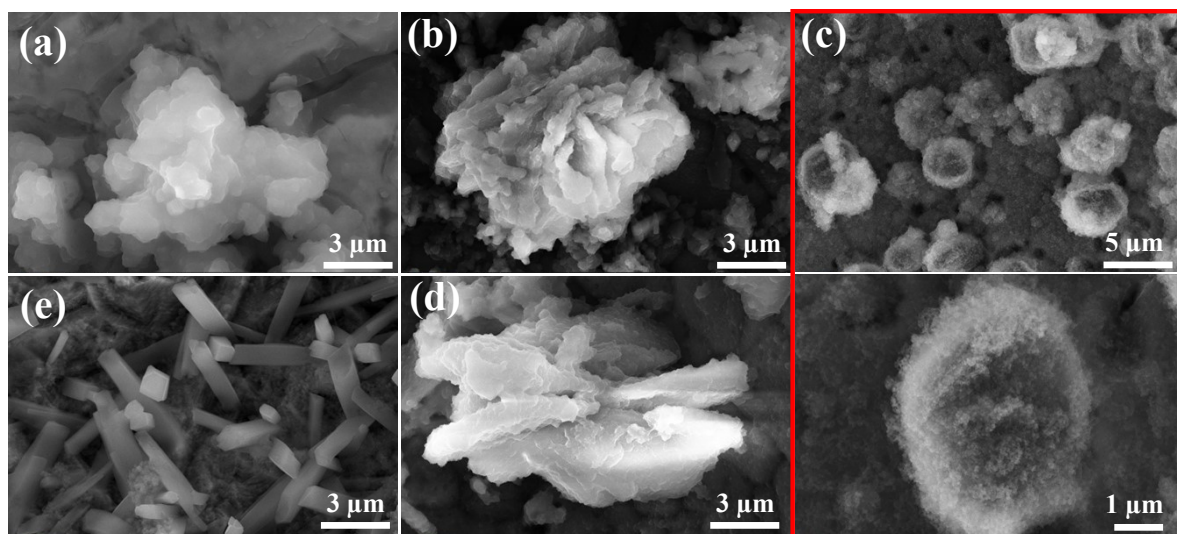
Fig. S21. SEM images of Fe-SACs|C-Ni@**1 (a)**, Fe-SACs|C-Ni@**2 (b)**, Fe-SACs|C-Ni@**3**, (c) Fe-SACs|C-Ni@**4** (d), and Fe-SACs|C-Ni@**5** (e) materials.

Fig. S22. LSV curves of the carbon-nickel (C-Ni) nanosheets electrode recorded in 1.0 M KOH at the scan rate of 10 mV s^{-1}.

Fig. S23. The isolated reduction peak of the same CV used for charge integration and the calculation of the number of active sites at the Fe-SACs|C-Ni@**3** electrode.
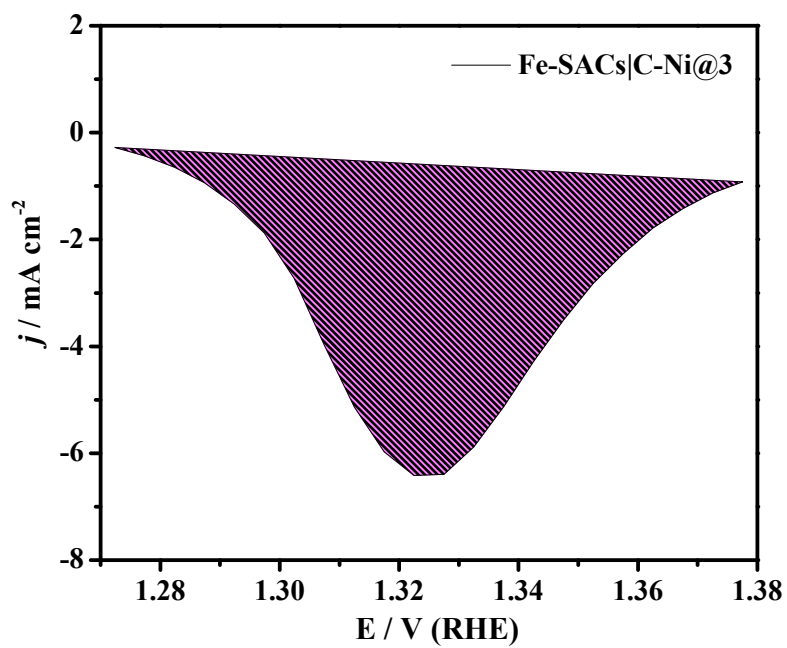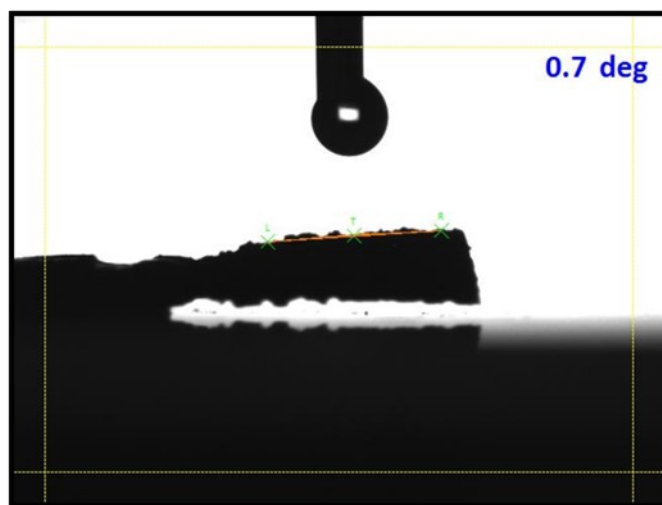
Fig. S24. Contact angle measurement of Fe-SACs|C-Ni@**3** catalyst after 50 h water electrolysis.
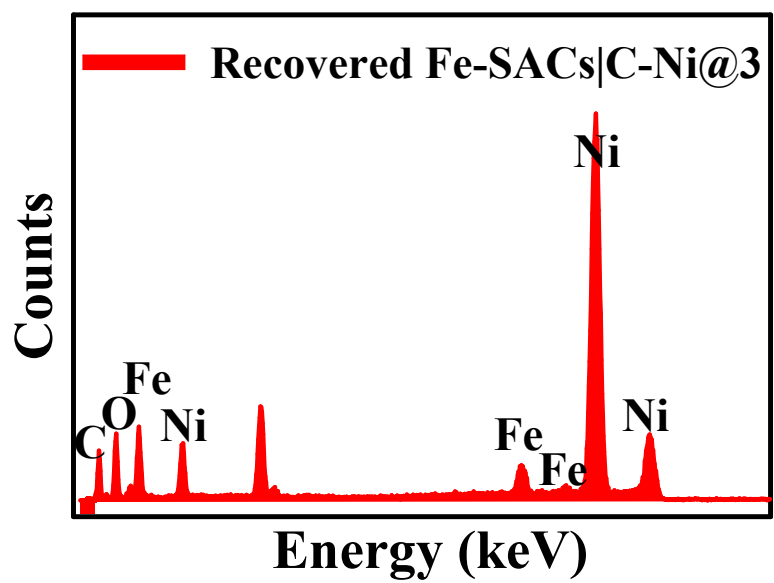
Fig. S25. EDX spectrum of recovered Fe-SACs|C-Ni@3 electrode.

References

1   B. Zhang, P. Huang, J. Chen, X. Dang, Y. Hu, Y. Ai, D. Zheng and H. Chen, *Applied Surface Science*, 2020, **504**, 144504.

2   S. Anantharaj, P. E. Karthik and S. Noda, *Angewandte Chemie International Edition*, 2021, **60**, 23051–23067.

3   B. Z. Desalegn, H. S. Jadhav and J. G. Seo, *Sustainable Energy & Fuels*, 2020, **4**, 1863–1874.

4   A. Shankar, R. Elakkiya and G. Maduraiveeran, *New Journal of Chemistry*, 2020, **44**, 5071–5078.

5   S. Arumugam, Y. Toku and Y. Ju, *Scientific Reports*, 2020, **10**, 5407.

6   N. Zhang, X. Feng, D. Rao, X. Deng, L. Cai, B. Qiu, R. Long, Y. Xiong, Y. Lu and Y. Chai, *Nature Communications*, 2020, **11**, 4066.

7   M. Lou Lindstrom, R. Gakhar, K. Raja and D. Chidambaram, *Journal of The Electrochemical Society*, 2020, **167**, 046507.

8   F. He, Y. Han, Y. Tong, M. Zhong, Q. Wang, B. Su and Z. Lei, *ACS Sustainable Chemistry & Engineering*, 2022, **10**, 6094–6105.

9   F. Paquin, J. Rivnay, A. Salleo, N. Stingelin and C. Silva-Acuña, *Journal of Materials Chemistry C*, 2015, **3**, 10715–10722.

10   A. Kumar and S. Bhattacharyya, *ACS Applied Materials & Interfaces*, 2017, **9**, 41906–41915.

11   H. Bian, T. Chen, Z. Chen, J. Liu, Z. Li, P. Du, B. Zhou, X. Zeng, J. Tang and C. Liu, *Electrochimica Acta*, 2021, **389**, 138786.

12   P. Wang, J. Zhu, Z. Pu, R. Qin, C. Zhang, D. Chen, Q. Liu, D. Wu, W. Li, S. Liu, J. Xiao and S. Mu, *Applied Catalysis B: Environmental*, 2021, **296**, 120334.

13   H. Shi, H. Liang, F. Ming and Z. Wang, *Angewandte Chemie International Edition*, 2017, **56**, 573–577.

14   J. Zheng, X. Chen, X. Zhong, S. Li, T. Liu, G. Zhuang, X. Li, S. Deng, D. Mei and J.-G. Wang, *Advanced Functional Materials*, 2017, **27**, 1704169.

15   C. Zhang, S. Bhoyate, P. K. Kahol, K. Siam, T. P. Poudel, S. R. Mishra, F. Perez, A. Gupta, G. Gupta and R. K. Gupta, *ChemNanoMat*, 2018, **4**, 1240–1246.

16   W.-H. Huang, X.-M. Li, X.-F. Yang, H.-B. Zhang, F. Wang and J. Zhang, *Chemical Communications*, 2021, **57**, 4847–4850.

17   S. M. Pawar, B. S. Pawar, B. Hou, J. Kim, A. T. Aqueel Ahmed, H. S. Chavan, Y. Jo, S. Cho, A. I. Inamdar, J. L. Gunjakar, H. Kim, S. Cha and H. Im, *Journal of Materials Chemistry A*, 2017, **5**, 12747–12751.

18   S. A. Khalate, S. A. Kadam, Y.-R. Ma, S. B. Kulkarni, V. G. Parale and U. M. Patil, *Journal of Colloid and Interface Science*, 2022, **613**, 720–732.